PCCP

ROYAL SOCIETY OF CHEMISTRY

PAPER

Cite this: *Phys. Chem. Chem. Phys.*, 2021, **23**, 1684

Oscillatory budding dynamics of a chemical garden within a co-flow of reactants†

D. Spanoudaki, Fabian Brau and A. De Wit *

Received 30th October 2020,
Accepted 3rd December 2020

DOI: 10.1039/d0cp05668e

rsc.li/pccp

The oscillatory growth of chemical gardens is studied experimentally in the budding regime using a co-flow of two reactant solutions within a microfluidic reactor. The confined environment of the reactor tames the erratic budding growth and the oscillations leave their imprint with the formation of orderly spaced membranes on the precipitate surface. The average wavelength of the spacing between membranes, the growth velocity of the chemical garden and the oscillations period are measured as a function of the velocity of each reactant. By means of materials characterization techniques, the micro-morphology and the chemical composition of the precipitate are explored. A mathematical model is developed to explain the periodic rupture of droplets delimitated by a shell of precipitate and growing when one reactant is injected into the other. The predictions of this model are in good agreement with the experimental data.

1 Introduction

Engineering strategies for designing functional materials with complex shapes are of fundamental interest in materials science. In particular, the design of hierarchical micro-structures with complex three-dimensional (3D) shapes is of interest for applications ranging from catalysis and optics to magnetic devices and sensing.[1–3]

A potential route for the controlled growth of 3D micro-structures is offered by precipitation reactions due to the diversity of 3D patterns they yield at various scales.[4,5] Among them, the self-organized precipitation of chemical gardens has recently attracted scientific attention due to the large variety of precipitation architectures they form.[6–8] Chemical gardens grow in out-of-equilibrium conditions by combination of osmosis and of the self-propagation of precipitation zones around a buoyancy-driven fluid flow. This leads to the emergence of complex morphologies with self-assembled layers of different chemical composition.[9] Understanding their rich chemical, electrical and magnetic properties related to the steep concentration and electrochemical gradients across their walls[10,11] is of tantamount interest in various fields including prebiotic chemistry[12,13] and catalysis.[6,8] Moreover, the self-organized growth mechanisms of chemical gardens are found in a plethora of natural systems such as in corrosion,[14–16] chimneys at hydrothermal vents,[17] cement hydration[18] and large-scale brinicles.[19] They serve thus as model systems to understand chemobrionics, *i.e.* the assembly of material architectures under a flux, and its exploitation in applications.[6,8]

The classical way to grow chemical gardens it to put a metal salt seed in a beaker containing a silicate solution. In that case, these gardens feature erratic shapes which are difficult to study both qualitatively and quantitatively. Indeed, the interplay between osmotic, buoyancy and reaction-diffusion processes induces in 3D a complex growth behavior. Various experimental approaches have been developed to control the growth of chemical gardens[7] such as starting from a controlled pellet seed[10,20,21] or using flow conditions. In these flow assisted techniques, experiments have focused on injecting a metal salt solution of known concentration in a 3D beaker of silicate[22–24] or phosphate,[25] and a quasi-2D Hele-Shaw cell (two glass plates separated by a thin gap).[26–30] More recently, flow conditions have been tested in microfluidic devices[31–33] or thin capillaries.[34] Growth properties have also been studied in presence of a bubble controlling the growth of tubular structures.[35,36]

When a chemical garden grows with injection of the metal salt solution in a 3D-reactor containing a stagnant solution of silicate, three distinct growth behaviors have been observed at a constant flow rate depending on the reactant concentrations.[22,23] In the *jetting* regime, observed at a low metal salt concentration, a buoyant jet of metal solution rises. Precipitation around that jet forms thin regular silica tubes. At a larger concentration, the *popping* regime is characterized by a periodic growth of the chemical garden. In this case, a membrane-bound droplet forms periodically at the tip of the silica tube. When the membrane ruptures, the droplet rises to the surface of the

Université libre de Bruxelles (ULB), Faculté des Sciences, Non Linear Physical Chemistry Unit, C. P. 231, 1050 Brussels, Belgium.
E-mail: adewit@ulb.ac.be

† Electronic supplementary information (ESI) available. See DOI: 10.1039/d0cp05668e

silicate solution and the process repeats itself. This oscillatory dynamics has been analyzed quantitatively and information has been extracted on the period of the oscillations, the growth velocities of the precipitation tubes, the critical volume needed to burst the droplet[22,23] and the chemical composition of the tubes.[24] A second transition towards a so-called *budding* regime is observed for larger metal salt concentrations. Under these conditions, the expanding droplet does not detach from the silica tube but rather bursts and nucleates a new droplet at the rupture site. The characterization and quantification of the budding oscillatory regime still remains a challenge due to the disordered growth of chemical gardens in the 3D container.

In this context, we study experimentally the growth of chemical gardens within the co-flow of cobalt chloride ($CoCl_2$) and sodium silicate (Na_2SiO_3) solutions in a microfluidic device for large reactant concentrations giving the budding regime in 3D. The reactor consists of two concentric capillaries that allow to control the relative speed at which the two reactants are put in contact by tuning the flow rate in each inlet capillary. Thanks to the confined space within the microfluidics capillaries and the co-flow, the oscillatory growth of the budding regime is tamed and gives periodically spaced membranes on the precipitate surface. A theoretical model is developed to explain the dependence of the pattern wavelength, of the velocity of the structure growth and of the period of oscillations on the velocities within the two flows. The chemical composition of these membranes is analyzed using standard materials characterization techniques such as X-ray Powder Diffraction (XRPD) and Energy Dispersive Spectroscopy (EDS). The micromorphology of the precipitates is studied by using optical microscopy and Scanning Electron Microscopy (SEM).

2 Materials and methods

Fig. 1 shows a schematic of the microfluidic reactor which consists of two vertical concentric capillaries forming a co-flow geometry. The capillaries of circular cross section are fluorinated ethylene propylene (FEP) chromatographic capillaries (Vici Jour). The dimensions of the outer FEP capillary are 3.2 mm for the outer diameter and d_{Si}^{in} = 2.1 mm for the inner diameter, whereas the dimensions of the inner FEP capillary are d_{Co}^{out} = 1.59 mm for the outer diameter and d_{Co}^{in} = 1.00 mm for the inner diameter. The two capillaries are connected using a commercially available Polyether Ether Ketone (PEEK) junction positioned vertically on a plexiglass plate. The injection of the reactants is carried out with a neMESYS low pressure syringe pump working with a BASE 120 controller. The preparation of 1.375 M $CoCl_2$ solution was done by dissolving $CoCl_2{\cdot}6H_2O$ (Sigma–Aldrich) in distilled water, whereas the Na_2SiO_3 was used as purchased (Sigma Aldrich), with a chemical composition: Na_2O = 10.6%, SiO_2 = 26.5%. The pH of the reactant solutions was measured with a pH benchtop meter inoLab pH7310. The experiments were recorded by an IDS CMOS camera (UI-3080CP-C-HQ R2). The samples are examined with an optical microscope Nikon SMZ18 and the photos of the

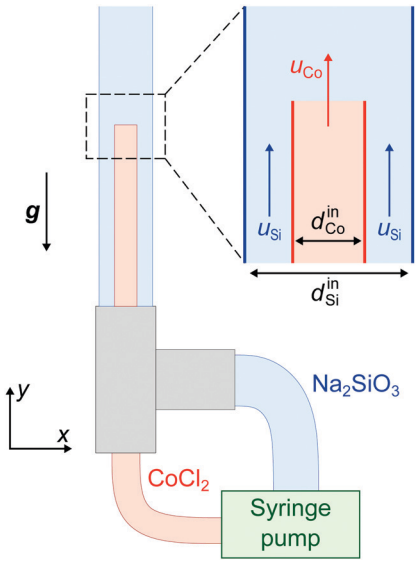

Fig. 1 Schematic of the microfluidic reactor.

samples were analyzed with the ImageJ software. Scanning Electron Microscopy (SEM) images were performed with a FEI QUANTA 200 3D microscope operated at 20.00 kV, coupled with an Energy Dispersive Spectroscopy detector with X-rays (EDX). A Bruker D8 Advance Diffractiometer with a coper anode as an X-ray source was used for X-ray Powder Diffraction (XRPD) measurements.

The range of flow rates used is 0.01–10 μL s^{-1}, as in similar studies with injection.[22–24,26–28] The velocity u_{Co} of the $CoCl_2$ solution in the capillary can be computed from the flow rate Q_{Co} imposed by the syringe pump using the following relation:

$$u_{Co} = \frac{4Q_{Co}}{\pi\left(d_{Co}^{in}\right)^2}. \quad (1)$$

Similarly, the velocity u_{Si} of the Na_2SiO_3 solution is computed as:

$$u_{Si} = \frac{4Q_{Si}}{\pi\left[\left(d_{Si}^{in}\right)^2 - \left(d_{Co}^{out}\right)^2\right]}, \quad (2)$$

where Q_{Si} is the flow rate of the Na_2SiO_3 solution.

3 Results and discussion

3.1 Qualitative observations

Let us first describe qualitatively the growth dynamics of the precipitate and the various patterns obtained when the $CoCl_2$ solution is injected either in a stagnant or in a flowing Na_2SiO_3 solution. A summary of the patterns observed and the parameter space of the problem spanned by the respective velocities of the cobalt and silicate solutions is shown in Fig. 2.

3.1.1 Stagnant Na_2SiO_3 solution. When the Na_2SiO_3 solution is stagnant (u_{Si} = 0 mm s^{-1}), two distinct growth behaviors are observed according to the $CoCl_2$ flow velocity. When $u_{Co} \leq 0.1$ mm s^{-1} (red circles in Fig. 2(c)), the

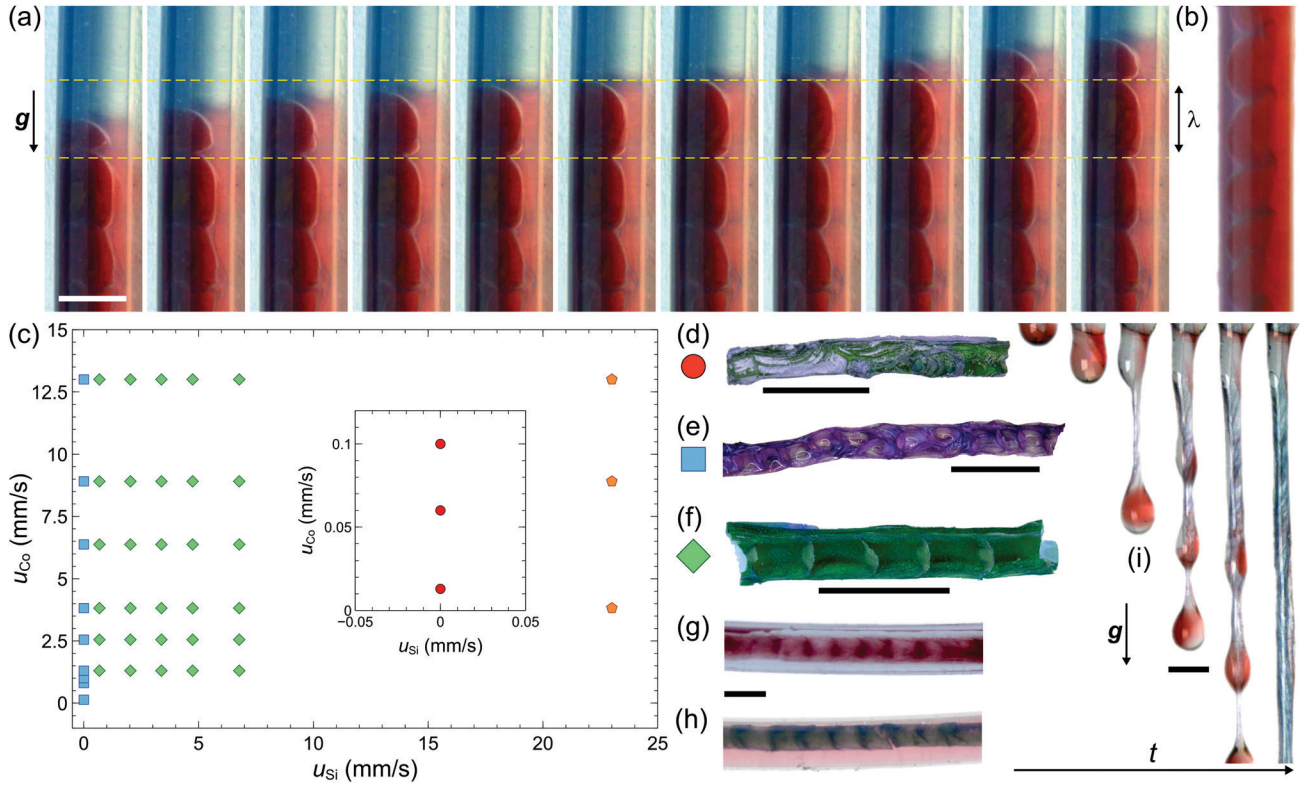

Fig. 2 (a) Periodic growth and rupture of a membrane-bound droplet filled of $CoCl_2$ injected upwards at a flow velocity u_{Co}= 3.82 mm s^{-1} within Na_2SiO_3 flowing at a velocity u_{Si} = 2.03 mm s^{-1}. Δt = 133 ms between two successive images. λ denotes the distance between the membranes. Scale bar: 3 mm. (b) Membrane-bound droplets filled of $CoCl_2$ injected at a flow velocity u_{Co} = 3.82 mm s^{-1} in a stagnant Na_2SiO_3 solution. (c) Phase diagram where u_{Co} and u_{Si} are, respectively, the flow velocity of the $CoCl_2$ and Na_2SiO_3 solutions. (d–f) Corresponding precipitates of the parameter space. Scale bar: 5 mm. (g and h) Chemical gardens obtained by using capillaries with smaller diameters in a stagnant Na_2SiO_3 solution: d^{in}_{Co} = 0.38 mm and d^{in}_{Si} = 1 mm. (g) u_{Co} = 1 mm s^{-1} and (h) u_{Co} = 2 mm s^{-1}. Scale bar: 1 mm. (i) Growth in time of a chemical garden acting as a microfluidic channel when solutions flow downwards outside the capillaries. u_{Co} = 12.7 mm s^{-1} and u_{Si} = 23 mm s^{-1}. Scale bar: 2 mm.

precipitation dynamics is essentially driven by buoyancy. Indeed, the density of the silicate solution is ρ_{Si} = 1.39 g ml^{-1} while that of the cobalt solution is ρ_{Co}= 1.15 g ml^{-1}. As the $CoCl_2$ solution is less dense and its injection speed so low, it rises by buoyancy within the stagnant denser silicate solution. As a result, like in 3D with no injection speed, the precipitate does not feature any regular pattern on its surface (Fig. 2(d)). When the $CoCl_2$ flow velocity increases, $u_{Co} > 0.1$ mm s^{-1} in the stagnant silicate (blue squares in Fig. 2(c)), the system enters the confined version of the oscillatory budding regime,[22,23] in which precipitation intermittently forms a membrane at the tip of the growing precipitate structure. Upon continuous injection of $CoCl_2$, the membrane of this $CoCl_2$ droplet bursts irregularly in time to release the injected fluid which reacts again to form a new expanding membrane-bound droplet. In addition, a lateral meandering is observed, and the precipitate spans the whole space available in the capillary (see Fig. 2(b) and Video S1, ESI†). This leaves its imprint on the surface of the precipitate with the formation of rather disordered membranes on it (Fig. 2(e)). The spatio-temporal dynamics in the budding regime seems however to be more regular in a confined geometry than in 3D. To test to what extent the confinement enhances the regularity of the precipitate morphology, we performed experiments of injection of $CoCl_2$ in stagnant silicate in capillaries with smaller outer and inner diameters. Fig. 2(g) and (h) show indeed that chemical gardens with ordered membranes form inside the microfluidic device in such a case. The confined space of the tubing microfluidics can thus reduce the growth complexity in the budding regime by reducing the available space in which the two fluid solutions react.

3.1.2 Flowing Na_2SiO_3 solution. The regularity of the frequency at which the $CoCl_2$ droplets rupture, and thus of the distance between precipitate membranes, can also be improved by using a co-flowing Na_2SiO_3 solution ($u_{Si} > 0$ mm s^{-1}) instead of reducing the system size. Fig. 2(a) and Video S2 (ESI†) show that the co-flow of the two reactant solutions reduces the available lateral space along the horizontal direction where the droplet grows. The volume inside the outer capillary splits then into two regions: an outer one (outside the membranes) where mainly Na_2SiO_3 flows and an inner one where mainly $CoCl_2$ flows and the droplet grows. This effect leads to an effective increase of the confinement which, as shown above, improves the overall regularity of the pattern imprinted in the precipitate as shown in Fig. 2(f) and 3(a). This behavior is observed for all green diamonds in Fig. 2(c).

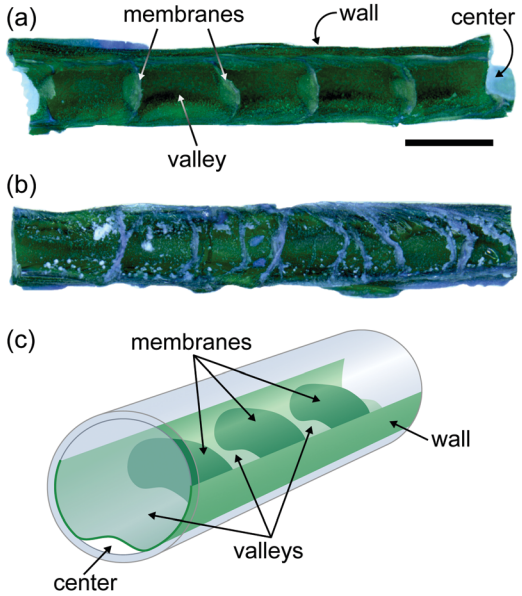

Fig. 3 Comparison of the patterns obtained under different $CoCl_2$ flow velocities, for steady u_{Si} = 2.03 mm s^{-1}. (a) u_{Co} = 1.27 mm s^{-1}, (b) u_{Co} = 8.91 mm s^{-1}. Scale bar: 2 mm. (c) Sketch of the regular precipitate structures observed in the co-flow system. Precipitate regions (membranes, valleys, center and wall) selected for the SEM analysis are also shown.

As a result, we obtain precipitates with membranes separated by a constant wavelength λ for given experimental conditions. Between two membranes, we observe a valley (see Fig. 3(a)), that corresponds to the interior of the growing bubble until a new membrane is formed at the given distance λ. As shown on Fig. 3(c), the sides of the precipitate structure growing on the capillary wall have a curved shape featuring a small indentation, called here "center", where the flow of sodium silicate mainly flows.

When the velocity of the cobalt is increased for moderate silicate velocity, the precipitates formed are more irregular and present a shorter wavelength between membranes (see Fig. 3(b)). If the velocity of the silicate is further increased, the precipitation reaction does not have time to grow a cohesive rigid shell and no regular structures are obtained. This behavior is observed typically for parameter values represented by the orange pentagons in Fig. 2(c) (see Video S3, ESI†).

Eventually, if the co-flow exits the capillaries, we observe that the reaction continues outside the capillaries in the atmospheric air. If the end of the outer capillary is twisted to let the two solutions drip down, the precipitate itself becomes a self-organized microfluidic reactor allowing the flow of both reactants. Fig. 2(i) and Video S4 (ESI†) show that, as the reaction proceeds, it leads to the formation of quite long precipitation tubes with regular formation of droplets that burst to let the tube continue to grow downwards in the gravity field.

3.1.3 Precipitate color. A closer observation of the tubes under the optical microscope shows different colors of the precipitate depending on the flow conditions. When u_{Si} = 0 mm s^{-1}, the precipitate displays a mix of purple and green colors where purple dominates (Fig. 2(d) and (e)). In contrast, for $u_{Si} > 0$ mm s^{-1}, the green color dominates (Fig. 2(f) and 3(a), (b)). This can be due to the different compositions around the growing precipitate depending whether the silicate flows or not. Moreover, during the aging of the samples occurring between the end of the experiment and the extraction of the precipitates for optical microscopy measurements, different chemical equilibria are reached with the precipitate depending whether $CoCl_2$ or silicate is more abundant around it, yielding different colors and chemical compositions.

3.2 Quantitative analysis

In a large part of the parameter space, regularly spaced membranes are obtained (see green diamonds in Fig. 2(c)). We analyze here quantitatively their properties. Specifically, we measure the average wavelength $\langle\lambda\rangle$ defined as the average distance between membranes, the growth velocity V of the precipitate and the characteristic time T_R between two consecutive rupture events of the membrane-bound droplets.

The average wavelength $\langle\lambda\rangle$ of the pattern was measured from optical microscopy images of numerous samples produced under co-flow conditions. Fig. 4(a) shows the dependence of $\langle\lambda\rangle$ on the $CoCl_2$ solution's velocity, u_{Co}. The variability of $\langle\lambda\rangle$ obtained from the 4 to 5 experiments performed under identical conditions is reflected in the error bars. For $u_{Co} <$ 4 mm s^{-1}, $\langle\lambda\rangle$ remains roughly constant, but at larger flow velocities, $\langle\lambda\rangle$ decreases linearly down to roughly half of its low flow velocity value for u_{Co} = 12.7 mm s^{-1}. Fig. 4(a) shows also the good agreement between the data and the prediction derived from a theoretical model developed in Section 4. Note that the average distance between membranes is here of the order of 1–2 mm, similar to the diameter of the tube. This is much larger than the characteristic wavelength of stripes observed on smaller tubes obtained by bubble-templated tubular growth.[35]

Fig. 4(b) shows that the velocity u_{Si} of the outer silicate flow does not have a significant effect on the pattern wavelength for all $CoCl_2$ velocities considered. Since $CoCl_2$ is filling the expanding droplet, we may indeed expect that its inner flow velocity has a larger impact on the dynamics than the outer flow velocity of Na_2SiO_3.

The growth velocity V of the tip of the precipitate was measured from images recorded with a high speed camera. Fig. 4(c) shows that the growth speed varies in first approximation linearly with u_{Co} for various u_{Si}. Increasing u_{Si} tends to slightly increase V. These results are similar to what is observed in the 3D popping regime of the oscillatory growth of chemical gardens[22] where the average growth also occurs at constant speed for given conditions.

Finally, knowing the average wavelength $\langle\lambda\rangle$ of the precipitate structure and the growth velocity V of the chemical gardens, the average time, T_R, between two rupture events can be calculated as $T_R = \langle\lambda\rangle/V$. In Fig. 4(d), we observe that T_R decreases when u_{Co} increases and is well described by the theoretical model developed in Section 4.

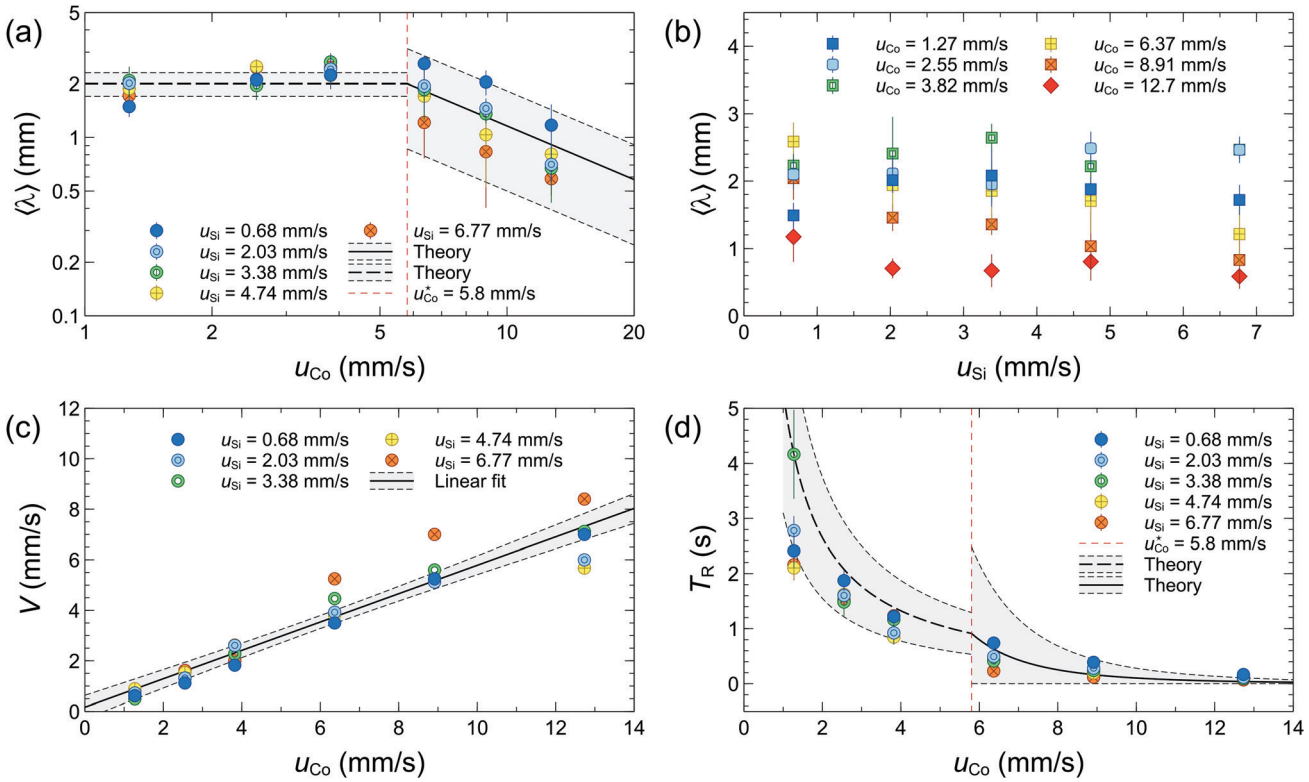

Fig. 4 (a) Log–log plot of the dependence of the average pattern wavelength, $\langle\lambda\rangle$, on the velocity u_{Co} (1 μL s^{-1} ≤ Q_{Co} ≤ 10 μL s^{-1}), for different velocities u_{Si}. The theoretical curves (20) and (24) obtained in Section 4 are also shown. (b) Average pattern wavelength $\langle\lambda\rangle$ as a function of u_{Si} for various u_{Co}. (c) Tube growth velocity, V, as a function of u_{Co} together with the linear fit $V = au_{Co} + b$ with a = 0.56 ± 0.03 and b = (0.17 ± 0.23) mm s^{-1}. (d) Average time between two rupture events, T_R, as a function of u_{Co} together with the theoretical curves (23) and (25) obtained in Section 4.

4 Mathematical modeling

The formation of a periodic structure in a co-flow geometry, when a reactant solution A ($CoCl_2$) is injected into a reactant solution B (Na_2SiO_3), is due to the periodic rupture of droplets filled of A and delimited by a shell of precipitate C, see Fig. 2(a). The experimental data reported in Fig. 4(b) show that the velocity of B has no significant impact on the pattern wavelength $\langle\lambda\rangle$. We will thus neglect it in the following.

We consider a spherical droplet filled of A and delimited by a shell of precipitate C. As shown experimentally previously,[23] the membrane-bound droplets growing at the tip of tubes when a metal salt solution is injected into silicate show essentially no leakage during the expansion phase. Hence, we can assume that the volume of the drop is directly proportional to the flow rate of the reactant A. The temporal evolution of the droplet volume, V, and area, S, are thus given by

$$V(t) = \frac{4\pi}{3}R(t)^3 = Q_{Co}t,\ S(t) = 4\pi R(t)^2, \tag{3}$$

where $R(t)$ is the radius of the sphere and Q_{Co} the volumetric flow rate of the reactant A. The temporal evolution of the droplet radius is thus given by

$$R(t) = [3Q_{Co}t/(4\pi)]^{1/3}. \tag{4}$$

The volume of the shell of precipitate is given by

$$V_p(t) = 4\pi R(t)^2 h(t), \tag{5}$$

where h is the thickness of the shell and $h/R \ll 1$. This assumption of thin shell is justified by the fact that, experimentally, the thickness of the membrane is much smaller than the wavelength $\lambda \simeq 2R$. The validity of this assumption is addressed in Appendix A. The average concentration of C in the shell is thus given by

$$\langle c\rangle(t) = \frac{n_C(t)}{V_p(t)} = \frac{n_C(t)}{4\pi R(t)^2 h(t)}, \tag{6}$$

where n_C is the number of moles of C. It has been shown[37] that, when A is injected radially into B in 3D, the total amount of C increases with t. Expressing the results by Comolli *et al.*[37] in dimensional units, we have the following scalings:

$$n_C(t) \underset{t<t_{ET}}{=} 1.166ka_0b_0D^{1/2}Q_{Co}^{2/3}t^{13/6}, \tag{7a}$$

$$n_C(t) \underset{t_{ET}<t<t_{TS}}{=} 1.314a_0 \ln\left[1+\frac{5\gamma}{2}\right]D^{1/2}Q_{Co}^{2/3}t^{7/6}, \tag{7b}$$

$$n_C(t) \underset{t>t_{TS}}{=} 0.088a_0Q_{Co}t, \tag{7c}$$

where a_0 and b_0 are the initial concentrations of A and B, $\gamma = b_0/a_0$, k is the kinetic constant of the reaction and D the diffusion coefficient assumed identical for all species. Therefore, to compare this theory to the experimental data, we consider D

as an effective parameter varying in the range $D = (2 \pm 1) \times 10^{-9}$ m^2 s^{-1} since most values of the diffusion coefficient in solution vary within this range.[38] t_{ET} and t_{TS} are, respectively, the times at which the transitions between the ''early-time'' and the ''transient'' regimes and between the ''transient'' and ''stationary'' regimes occur.[37] The expressions of t_{ET} and t_{TS} are obtained, respectively, by equating eqn (7a) to eqn (7b) and eqn (7b) to eqn (7c):

$$t_{ET} = \frac{1.127}{kb_0}\ln(1 + 5\gamma/2), \quad t_{TS} = \frac{9.02 \times 10^{-8}}{\ln^6(1 + 5\gamma/2)}\frac{Q_{Co}^2}{D^3}. \qquad (8)$$

The reaction considered in this work is very fast since it can form solid tubes under rather high injection rate (Q_{Co} = 0.11 mL s^{-1}) in a quasi-2D geometry.[26] Assuming $k > 10$ L mol^{-1} s^{-1} and $D \simeq 2 \times 10^{-9}$ m^2 s^{-1} and using the initial concentration of the reactants, a_0 = 1.375 M and b_0 = 6.25 M, we then get

$$t_{ET} < 4.5 \times 10^{-2} \text{ s}, \quad t_{TS} \simeq (5 \times 10^{16} \text{ s}^3 \text{ m}^{-6})Q_{Co}^2. \qquad (9)$$

Consequently, t_{TS} varies between 0.05 s and 5 s when Q_{Co} varies between 1 μl s^{-1} and 10 μl s^{-1} as in the experiments performed to measure the average wavelength of the pattern, see Fig. 4(a). As shown quantitatively below, this significant variation of t_{TS} when Q_{Co} varies within its experimental range explains the transition observed in the evolution of $\langle\lambda\rangle$ with u_{Co} reported in Fig. 4(a). Indeed, at Q_{Co} = 1 μl s^{-1} ($t_{TS} \simeq 0.05$ s), the rupture of the shell occurs at a time $T_R > t_{TS}$ such that n_C is given by eqn (7c), whereas at Q_{Co} = 10 μl s^{-1} ($t_{TS} \simeq 5$ s), the rupture of the shell occurs at a time $t_{ET} < T_R < t_{TS}$ so that n_C is then given by eqn (7b).

4.1 Main equation

A sheet of a given material is characterized by a work of fracture, Σ, which represents the energy per unit area required to make a crack grow in the sheet. In other words, the energy required to make a crack move by a distance ℓ is $\Sigma h\ell$ where h is the thickness of the sheet.[39] In our case, the properties of the material composing the precipitate shell change during the growth of the droplet[20] filled by the reactant A since the concentration of C increases with time, see eqn (7). Therefore, we expect that the work of fracture varies with the concentration of C: $\Sigma = \Sigma(c)$. Here, we assume that this dependence on c is linear

$$\Sigma = \eta\langle c\rangle, \qquad (10)$$

where η is a constant with units N L (m mol)$^{-1}$. Note that a rupture can only occur if the precipitate is sufficiently cohesive. At short time, of the order of t_{ET}, the amount of precipitate located between the two reactive solutions of A and B is still small. Therefore, we don't expect any rupture process within such a short time in agreement with the characteristic time between two rupture events observed experimentally, see Fig. 4(d). Consequently, it is expected that the concept of work of fracture and eqn (10) apply only at sufficiently large times ($t > t_{ET}$).

When the volume of the droplet grows by an amount dV, a crack of length dR appears in the shell when the work performed by the fluid pressure is equal to the work of fracture:

$$P\mathrm{d}V = \Sigma h\mathrm{d}R = \eta\langle c\rangle h\mathrm{d}R, \qquad (11)$$

where P is the pressure difference across the shell. Using dV = $4\pi R^2$dR and eqn (6), we get

$$16\pi^2 R(t)^4 P = \eta n_C(t). \qquad (12)$$

4.2 Wavelength and rupture time

The wavelength observed in the precipitate structure and reported in Fig. 4(a) is computed as the diameter of the droplet when the rupture occurs. As explained above, we expect that a rupture event takes place when $t_{ET} < t < t_{TS}$ at high flow rate or $t > t_{TS}$ at low flow rate.

4.2.1 Low flow rate. Eqn (9) shows that t_{TS} is small at low flow rates Q_{Co}. The rupture time, T_R, is thus expected to be larger than t_{TS} in this case. Therefore, n_C is given by eqn (7c) which, together with (12), gives

$$16\pi^2 R(t)^4 P = 0.088\eta a_0 Q_{Co} t. \qquad (13)$$

Using the expression (4) of R and solving for t, we obtain the rupture time

$$T_R = 5.33 \times 10^{-8}\frac{\eta^3 a_0^3}{P^3 Q_{Co}}. \qquad (14)$$

As shown in Fig. 2(a), the distance λ between two successive membranes is equal to the diameter of the membrane-bound droplet filled of $CoCl_2$ when it ruptures. Since the droplet is assumed to be a growing sphere of radius R given by (4), the wavelength λ is equal to the diameter ($2R$) of the droplet evaluated at the time T_R when a rupture event occurs. The pattern wavelength is thus given by

$$\lambda \simeq 2R(T_R) = 4.7 \times 10^{-3}\frac{\eta a_0}{P}. \qquad (15)$$

The wavelength is thus constant at sufficiently low flow rates $Q_{Co} < Q_{Co}^*$. The value of Q_{Co}^* is computed below.

4.2.2 Large flow rate. At larger flow rates, the rupture time, T_R, is expected to be smaller than t_{TS} (but still larger than t_{ET}). Therefore, n_C is given by Eqn (7b), and together with (12), we get

$$16\pi^2 R(t)^4 P = 1.314\eta a_0 \ln[1 + 5\gamma/2]D^{1/2}Q_{Co}^{2/3}t^{7/6}. \qquad (16)$$

Using the expression (4) of R and solving for t, the rupture time is found to be

$$T_R = 3.15 \times 10^{-8}\frac{\eta^6 a_0^6 D^3 \ln^6(1 + 5\gamma/2)}{P^6 Q_{Co}^4}. \qquad (17)$$

The pattern wavelength is thus given by

$$\lambda \simeq 2R(T_R) = 3.9 \times 10^{-3}\left[\frac{\eta a_0}{P}\right]^2 \ln^2(1 + 5\gamma/2)DQ_{Co}^{-1}. \qquad (18)$$

The wavelength is thus inversely proportional to the flow rate at sufficiently large flow rates $Q_{Co} > Q_{Co}^*$ or, equivalently, at

sufficiently large flow velocities according to eqn (1). The transition between the two regimes occurs at a flow rate obtained by equating the two expressions (15) and (18) of the wavelength:

$$Q^{*}_{\mathrm{Co}} = 0.84\frac{\eta a_0}{P} D \ln^2(1 + 5\gamma/2). \quad (19)$$

4.3 Comparison with experiments

Since the parameter η is not known, we use the experimental value of the wavelength at low flow rates, $u_{\mathrm{Co}} \leq 3.82$ mm s^{-1}, to determine it:

$$\lambda_{\mathrm{exp}} = (2.0 \pm 0.3)\ \mathrm{mm}. \quad (20)$$

Using this value of the wavelength in eqn (15), we obtain

$$\frac{\eta a_0}{P} = (4.3 \pm 0.6) \times 10^2 \mathrm{mm}. \quad (21)$$

Using this value in eqn (14), we obtain the rupture time at low flow rates

$$T_{\mathrm{R}} = \frac{(4.2 \pm 1.8)\ \mu\mathrm{L}}{Q_{\mathrm{Co}}}, \quad (22)$$

where Q_{Co} is measured in μL s^{-1}. To better compare to the experimental data reported in Fig. 4(d), we use eqn (1) together with $d^{\mathrm{in}}_{\mathrm{Co}} = 1$ mm to express T_{R} as a function of u_{Co}:

$$T_{\mathrm{R}} = \frac{(5.3 \pm 2.2)\ \mathrm{mm}}{u_{\mathrm{Co}}}, \quad (23)$$

where u_{Co} is expressed in mm s^{-1}. Eqn (23) agrees well with the data reported in Fig. 4(d) without any fitting parameter.

The pattern wavelength and the rupture time can now be computed at large flow rates. Using eqn (21) in eqn (18) together with $D = (2 \pm 1) \times 10^{-9}$ m^2 s^{-1} and $\gamma = b_0/a_0 = 4.55$, the theoretical value of the wavelength at large flow rates reads

$$\lambda_{\mathrm{th}} = \frac{(9.1 \pm 5.2)\ \mathrm{mm}^4\ \mathrm{s}^{-1}}{Q_{\mathrm{Co}}} = \frac{(11.6 \pm 6.6)\ \mathrm{mm}^2\ \mathrm{s}^{-1}}{u_{\mathrm{Co}}}, \quad (24)$$

where Q_{Co} and u_{Co} are expressed in μL s^{-1} and mm s^{-1} respectively and where we used eqn (1) to express λ_{th} as a function of u_{Co}. Eqn (24) agrees well with the data reported in Fig. 4(a).

Using eqn (21) in eqn (17) together with the values of D and γ reported above, we obtain the rupture time at large flow rates

$$T_{\mathrm{R}} = \frac{\left(393^{+677}_{-393}\right)\ \mu\mathrm{L}^4\ \mathrm{s}^{-3}}{Q^4_{\mathrm{Co}}} = \frac{\left(1034^{+1778}_{-1034}\right)\ \mathrm{mm}^4\ \mathrm{s}^{-3}}{u^4_{\mathrm{Co}}}, \quad (25)$$

where again Q_{Co} and u_{Co} are expressed in μL s^{-1} and mm s^{-1} respectively and where we used eqn (1) to express T_{R} as a function of u_{Co}. Eqn (25) agrees again well with the data reported in Fig. 4(d) without any fitting parameter.

The flow rate at which the transition between the two regimes occurs is obtained by using eqn (19) and (21) with the values of D and γ reported above:

$$Q^{*}_{\mathrm{Co}} = (4.5 \pm 0.7)\ \mu\mathrm{L\ s}^{-1}. \quad (26)$$

The corresponding flow velocity is found by using eqn (1) with the value of $d^{\mathrm{in}}_{\mathrm{Co}}$ used above:

$$u_{\mathrm{Co}}{}^{\star} = (5.8 \pm 0.9)\ \mathrm{mms}^{-1}. \quad (27)$$

This value of the flow velocity compares well with the velocity at which the transition is observed experimentally, see Fig. 4(a).

Finally, the force Σh required to make a crack propagate in the shell of precipitate can be estimated using eqn (10) together with Eqn (4) and (6). For example, in the regime where the wavelength is constant and at the rupture time $t = T_{\mathrm{R}}$ given by eqn (14), we obtain

$$\Sigma h = \frac{\eta n_{\mathrm{C}}(T_{\mathrm{R}})}{4\pi R(T_{\mathrm{R}})^2} = 6.8 \times 10^{-5}\left[\frac{\eta a_0}{P}\right]^2 P \simeq 10^{-2} N, \quad (28)$$

where we used Eqn (23) and $P \simeq 1$ kPa.[40]

5 *Ex situ* materials characterization

Materials characterization techniques, such as scanning electron microscopy (SEM), X-ray diffraction (XRD) and Energy-dispersive X-ray spectroscopy (EDX) were employed to analyze the micro-morphology of the self-organized precipitates and their chemical composition.

Two regions on the precipitate are considered for the SEM analysis (see Fig. 3(c)): the ''upper part'' of the precipitate structure where the membranes are separated by valleys and the ''back'' of the precipitate structure where the center is surrounded by the solid phase in contact with the capillary walls. In the upper part, the cobalt dominates in the valleys while the back side of the precipitate is, in contrast, rather poor in cobalt.

The upper part is divided in two subregions: the membranes and the valleys between two membranes. The SEM images of Fig. 5(a) and (b) show the presence of wavy structures on the top of the membrane, *i.e.* the macroscopic membranes contain numerous micro-membranes.[41] The EDX analysis (Table 1) suggests that the elements of all the involved chemical reactants can be found in the membranes. SEM images of a valley between the two membranes (Fig. 5(c) and (d)) show that microspheres are formed there during the precipitation. The EDX analysis (Table 1) shows that the cobalt is by far the most abundant element in these valleys between the membranes.

In the center of the back of the precipitate (Fig. 5(e) and (f)), where the sodium silicate flows during the experiment, a porous structure has been formed with a pore size smaller than 10 μm. The walls of the back part (Fig. 5(g) and (h)) have, in contrast, a more compact micro-structure than the center. This region may have been influenced by the capillary wall. The EDX analysis (Table 1) suggests that the back of the precipitate has an elemental composition similar to the membranes of the upper part.

The crystallinity of the precipitate has been explored using the XRD technique. The XRD spectrum presented in Fig. 6 shows a highly amorphous precipitate with a weak peak at 11 deg., probably caused by cobalt nanoparticles, and is similar to previous XRD spectra of silica gardens grown from pressed pellets of $CoCl_2{\cdot}6H_2O$.[42]

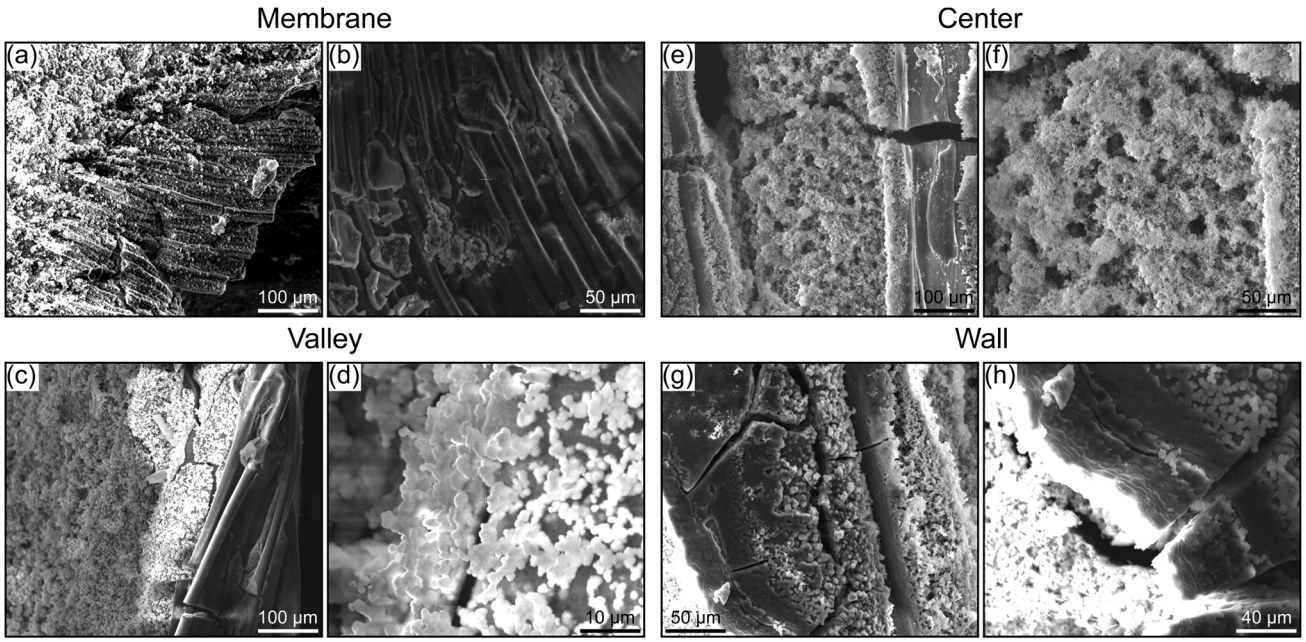

Fig. 5 Scanning Electron Microscopy images of various precipitate regions. (a) and (b) Membrane. (c) and (d) Valley between two membranes. (e and f) Center and (g and h) wall parts of the back the tubes. Samples obtained for u_{Co} = 1.27 mm s^{-1} and u_{Si} = 2.03 mm s^{-1}.

Table 1 EDX analysis of a membrane, valley and the back of the precipitate

Membrane		Valley		Back	
Element	Weight%	Element	Weight%	Element	Weight%
O	29.47	Co	96.49	O	39.32
Na	15.33	Cl	2.18	Na	12.66
Si	36.15	Si	1.33	Si	31.30
Cl	13.59			Cl	12.16
Co	5.46			Co	3.96

Based on the chemistry of the cobalt–silicate chemical gardens[43] and compositional analysis of chemical garden precipitation tubes grown in flow conditions,[24] we can understand the composition of the upper zone (Table 1) and the XRD measure of mainly amorphous material as follows. The membranes mainly formed of $CoO{\cdot}xSiO_2$ are rich in both cobalt, silicate and oxygen. They separate the acidic solution of the metal salt (pH = 4.24) from the basic silicate solution (pH = 11.55). H^+ cations diffuse through the membrane from the metal salt side to the silicate side and decrease locally the pH. This causes the precipitation of amorphous silica on the outer wall, which explains the X-ray diffraction pattern of Fig. 6. On the metal salt side, the increase of pH due to the rapid diffusion of OH^- anions from the alkaline silicate side causes the formation of colloidal metal hydroxide $Co(OH)_2$.[24,44,45]

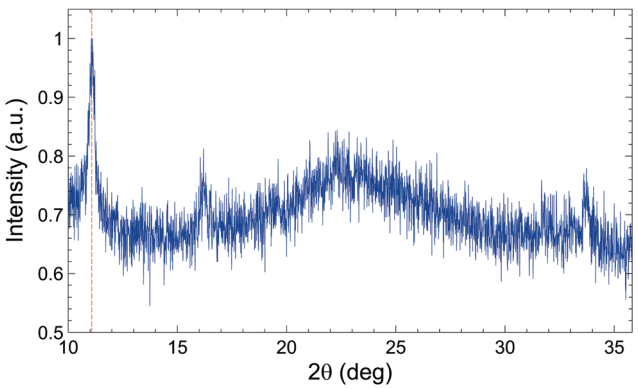

Fig. 6 X-ray diffraction pattern. Scan rate: 0.05° min^{-1}. Sample taken for u_{Co} = 1.27 mm s^{-1} and u_{Si} = 2.03 mm s^{-1}.

6 Conclusions

The oscillatory precipitation of a chemical garden has been studied experimentally in a microfluidic co-flow reactor by injecting a solution of cobalt chloride at a given velocity within a flowing solution of silicate. We have analysed the formation of patterned precipitation tubes for high reactant concentrations for which a budding oscillatory regime is observed when the cobalt solution is injected into a 3D beaker of stagnant silicate.[22,23] We find that the confinement and the co-flow of reactants both tame the irregular bursting growth to yield membranes rich in all reactant elements periodically separated by valleys rich in cobalt on the upper side of the tubes. The back of the precipitate structure shows a chemical composition similar to the membranes. The wavelength between membranes is roughly 2 mm up to a cobalt solution velocity u_{Co} of the order of 5 mm s^{-1} while a decrease in the wavelength is observed at larger u_{Co}. The spacing between membranes becomes also more irregular at large u_{Co}. The wavelength is found to be independent of the silicate solution's velocity u_{Si}. The chemical garden tube's growth velocity V increases linearly with u_{Co} while the average time between two rupture events of

the growing membrane decreases as u_{Co} increases. XRD measurements show the presence of a highly amorphous precipitate that can be explained by the chemistry of chemical gardens, whereas SEM images reveal a hierarchical substructure of smaller size membrane on the macroscopic membranes.

A mathematical model has been developed based on the periodic growth of a spherical membrane when a solution of cobalt is injected into a solution of silicate. When reaching a given radius, the membrane bursts and a new membrane starts to grow. Expressing the work of fracture as a function of the average concentration of the solid product allows to compute a rupture time. At low flow rate, this rupture time decreases as ${u_{Co}}^{-1}$ yielding a constant wavelength while at larger flow rates, $u_{Co} > 5$ mm s^{-1}, the rupture time decreases as ${u_{Co}}^{-4}$ inducing a wavelength that is inversely proportional to the flow rate. The analytical expressions are in good agreement with the experimental data.

Our results show that microfluidic co-flow geometries provide a good tool to control the growth of regularly templated chemical garden tubes. This paves the way to further experimental and theoretical studies of engineering techniques for the controlled growth of solid tubes with interesting material properties.

Conflicts of interest

There are no conflicts to declare.

A Thin shell hypothesis

The model presented in the main text did not require any hypothesis on the shell thickness except it is small compared to the radius of the shell. The shell is composed of the precipitate generated by the reaction between the two reactive fluids A and B. Therefore, the product C is produced in the depletion zone where A and B are consumed by the reaction. This region is known to grow diffusively independently of the geometry.[46,47] Assuming that $h \sim (Dt)^{1/2}$, we can compute h/R in the two regimes at the rupture time T_R.

A.1 Low flow rate

Using the expression (4) of R evaluated at $t = T_R$ given by eqn (14), we obtain

$$\frac{h(T_R)}{R(T_R)} = 9.9 \times 10^{-2}\left[\frac{\eta a_0}{P}\right]^{1/2}\left[\frac{D}{Q_{Co}}\right]^{1/2}. \quad (29)$$

Using the mean value eqn (21), we have

$$\frac{h(T_R)}{R(T_R)} = 6.5 \times 10^{-2}\left[\frac{D}{Q_{Co}}\right]^{1/2}. \quad (30)$$

Using $D = 2 \times 10^{-9}$ m^2 s^{-1}, the ratio h/R varies between 0.09 and 0.03 at the rupture time when Q_{Co} varies between 1 and 10 μl s^{-1}.

A.2 Large flow rate

Using the expression (4) of R evaluated at $t = T_R$ given by eqn (17), we obtain

$$\frac{h(T_R)}{R(T_R)} = 9.1 \times 10^{-2}\left[\frac{\eta a_0}{P}\right]\left[\frac{D}{Q_{Co}}\right]\ln\left[1+\frac{5\gamma}{2}\right]. \quad (31)$$

Using the mean value eqn (21), we have

$$\frac{h(T_R)}{R(T_R)} = 3.9 \times 10^{-2}\left[\frac{D}{Q_{Co}}\right]\ln\left[1+\frac{5\gamma}{2}\right]. \quad (32)$$

Using $D = 2 \times 10^{-9}$ m^2 s^{-1} and $\gamma = 4.55$, the ratio h/R varies between 0.20 and 0.02 at the rupture time when Q_{Co} varies between 1 and 10 μl s^{-1}.

Acknowledgements

The authors acknowledge support by F. R. S. – FNRS under the M-ERA.NET Grant No. R. 50.12.17.F. We thank Didier Robert for SEM – EDX measurements, and Yves Geerts, Guangfeng Liu and Jie Liu for XRD measurements.

References

1 B. Lim, M. Jiang, P. H. C. Camargo, E. C. Cho, J. Tao, X. Lu, Y. Zhu and Y. Xia, *Science*, 2009, **324**, 1302–1305.
2 J. K. Gansel, M. Thiel, M. S. Rill, M. Decker, K. Bade, V. Saile, G. von Freymann, S. Linden and M. Wegener, *Science*, 2009, **325**, 1513–1515.
3 W. Jia, L. Su and Y. Lei, *Biosens. Bioelectron.*, 2011, **30**, 158–164.
4 E. Nakouzi and O. Steinbock, *Sci. Adv.*, 2016, **2**, e1601144.
5 W. L. Noorduin, A. Grinthal, L. Mahadevan and J. Aizenberg, *Science*, 2013, **340**, 832–837.
6 L. M. Barge, S. S. S. Cardoso, J. H. E. Cartwright, G. J. T. Cooper, L. Cronin, A. De Wit, I. J. Doloboff, B. Escribano, R. E. Goldstein, F. Haudin, *et al.*, *Chem. Rev.*, 2015, **115**, 8652–8703.
7 R. Makki, L. Roszol, J. J. Pagano and O. Steinbock, *Philos. Trans. R. Soc., A*, 2012, **370**, 2848–2865.
8 S. S. S. Cardoso, J. H. E. Cartwright, J. Cejková, L. Cronin, A. De Wit, S. Giannerini, D. Horváth, A. Rodrigues, M. Russell, C. Sainz-Diaz and A. Tóth, *Artif. Life*, 2020, **26**, 315–326.
9 J. H. E. Cartwright, J. M. García-Ruiz, M. L. Novella and F. Otálora, *J. Colloid Interface Sci.*, 2002, **256**, 351–359.
10 F. Glaab, M. Kellermeier, W. Kunz, E. Morallon and J. M. García-Ruiz, *Angew. Chem.*, 2012, **51**, 4317–4321.
11 L. M. Barge, Y. Abedian, M. J. Russell, I. J. Doloboff, J. H. E. Cartwright, R. D. Kidd and I. Kanik, *Angew. Chem.*, 2015, **54**, 8184–8187.
12 R. Saladino, G. Botta, B. M. Bizzarri, E. D. Mauro and J. M. García-Ruiz, *Biochemistry*, 2016, **55**, 2806–2811.
13 B. M. Bizzarri, L. Botta, M. I. Pérez-Valverde, R. Saladino, E. D. Mauro and J. M. García-Ruiz, *Chem. – Eur. J.*, 2018, **24**, 8126–8132.

14 F. Brau, F. Haudin, S. Thouvenel-Romans, A. De Wit, O. Steinbock, S. S. S. Cardoso and J. H. E. Cartwright, *Phys. Chem. Chem. Phys.*, 2018, **20**, 784–793.

15 F. Brau, S. Thouvenel-Romans, O. Steinbock, S. S. S. Cardoso and J. H. E. Cartwright, *Soft Matter*, 2019, **15**, 803–812.

16 G. Butler and H. C. K. Ison, *Nature*, 1958, **182**, 1229–1230.

17 J. B. Corliss, J. Dymond, L. I. Gordon, J. M. Edmond, R. P. von Herzen, R. D. Ballard, K. Green, D. Williams, A. Bainbridge, K. Crane and T. H. van Andel, *Science*, 1979, **203**, 1073–1083.

18 D. D. Double and A. Hellawell, *Nature*, 1976, **261**, 486–488.

19 J. H. E. Cartwright, B. Escribano, D. L. González, C. I. Sainz-Díaz and I. Tuval, *Langmuir*, 2013, **29**, 7655–7660.

20 J. Pantaleone, A. Tóth, D. Horváth, J. Rother McMahan, R. Smith, D. Butki, J. Braden, E. Mathews, H. Geri and J. Maselko, *Phys. Rev. E: Stat., Nonlinear, Soft Matter Phys.*, 2008, **77**, 046207.

21 P. Kumar, D. Horváth and A. Tóth, *Soft Matter*, 2020, **5**, 8325–8329.

22 S. Thouvenel-Romans and O. Steinbock, *J. Am. Chem. Soc.*, 2003, **125**, 4338–4341.

23 S. Thouvenel-Romans, W. van Saarloos and O. Steinbock, *Europhys. Lett.*, 2004, **67**, 42–48.

24 J. J. Pagano, S. Thouvenel-Romans and O. Steinbock, *Phys. Chem. Chem. Phys.*, 2007, **9**, 110–116.

25 A. Tóth, D. Horváth, R. Smith, J. R. McMahan and J. Maselko, *J. Phys. Chem. C*, 2007, **111**, 14762–14767.

26 F. Haudin, J. H. E. Cartwright, F. Brau and A. De Wit, *Proc. Natl. Acad. Sci. U. S. A.*, 2014, **111**, 17363–17367.

27 F. Haudin, J. H. E. Cartwright and A. De Wit, *J. Phys. Chem. C*, 2015, **119**, 15067–15076.

28 F. Haudin, V. Brasiliense, J. H. E. Cartwright, F. Brau and A. De Wit, *Phys. Chem. Chem. Phys.*, 2015, **17**, 12804–12811.

29 S. Wagatsuma, T. Higashi, Y. Sumino and A. Achiwa, *Phys. Rev. E*, 2017, **95**, 52220.

30 Q. Wang, M. R. Bentley and O. Steinbock, *J. Phys. Chem. C*, 2020, **124**, 21617–21624.

31 B. C. Batista and O. Steinbock, *J. Phys. Chem. C*, 2015, **119**, 27045–27052.

32 Q. Wang, F. M. Zanotto and O. Steinbock, *J. Phys. Chem. C*, 2017, **121**, 14120–14127.

33 Y. Ding, J. H. E. Cartwright and S. S. S. Cardoso, *Phys. Rev. Fluids*, 2020, **16**, 082201(R).

34 P. Knoll, A. V. Gonzalez, Z. C. McQueen and O. Steinbock, *Chem. – Eur. J.*, 2019, **25**, 13885–13889.

35 S. Thouvenel-Romans, J. J. Pagano and O. Steinbock, *Phys. Chem. Chem. Phys.*, 2005, **7**, 2610.

36 D. A. Stone and R. E. Goldstein, *Proc. Natl. Acad. Sci. U. S. A.*, 2004, **101**, 11537–11541.

37 A. Comolli, A. De Wit and F. Brau, *Phys. Rev. E*, 2019, **100**, 052213.

38 P. Vanýsek, in *CRC Handbook of Chemistry and Physics*, ed. D. R. Lide, CRC Press/Taylor and Francis, Boca Raton, 90th edn, 2010, ch. 5, p. 76.

39 E. Hamm, P. Reis, M. LeBlanc, B. Roman and E. Cerda, *Nat. Mater.*, 2008, **7**, 386–390.

40 J. Pantaleone, A. Tóth, D. Horváth, L. RoseFigura, W. Morgan and J. Maselko, *Phys. Rev. E: Stat., Nonlinear, Soft Matter Phys.*, 2009, **79**, 056221.

41 R. Lakes, *Nature*, 1993, **361**, 511.

42 F. Glaab, J. Rieder, R. Klein, D. Choquesillo-Lazarte, E. Melero-Garcia, J. M. García-Ruiz, W. Kunz and M. Kellermeier, *ChemPhysChem*, 2017, **18**, 338–345.

43 D. Balköse, F. Özkan, U. Köktürk, S. Ulutan, S. Ülkü and G. Nisli, *J. Sol–Gel Sci. Technol.*, 2002, **23**, 253–263.

44 Z. Liu, R. Ma, M. Osada, K. Takada and T. Sasaki, *J. Am. Chem. Soc.*, 2005, **127**, 13869–13874.

45 J. Maselko and P. Strizhak, *J. Phys. Chem. B*, 2004, **108**, 4937–4939.

46 L. Gálfi and Z. Rácz, *Phys. Rev. A: At., Mol., Opt. Phys.*, 1988, **38**, 3151(R)–3154(R).

47 F. Brau, G. Schuszter and A. De Wit, *Phys. Rev. Lett.*, 2017, **118**, 134101.